

Measurements of the Directional Spectrum across the Equilibrium Saturation Ranges of Wind-Generated Surface Waves

LUC LENAIN AND W. KENDALL MELVILLE

Scripps Institution of Oceanography, University of California, San Diego, La Jolla, California

(Manuscript received 30 January 2017, in final form 23 May 2017)

ABSTRACT

It is now well accepted that to better understand the coupling between the atmosphere and the ocean, and improve coupled ocean–atmosphere models, surface wave processes need to be taken into account. Here, properties of the directional distributions of the surface wave field across the equilibrium and saturation ranges are investigated from airborne lidar data collected during the ONR Southern California 2013 (SoCal2013) experiment, conducted off the coast of Southern California in November 2013. During the field effort, detailed characterization of the marine atmospheric boundary layer was performed from Research Platform (R/P) *Floating Instrument Platform (FLIP)*, moored at the center of the aircraft operational domain. The wind speed ranged from approximately 1–2 to up to 11 m s⁻¹, while the significant wave height varied from 0.8 to 2.5 m during the 10 days of data collection considered in the analysis. The directional wavenumber spectrum exhibits a clear, bimodal distribution that extends well beyond what was reported in previous studies, with the azimuthal separation between the lobes reaching $\approx \pi$ for the highest wavenumbers that could be resolved: approximately 10–12 rad m⁻¹. The results demonstrate that opposing wave components can be found in one storm system rather than requiring waves from opposing storms, with implications for ocean acoustics. With the broad wavenumber range of the directional spectra obtained from the lidar, the transition from the equilibrium to saturation ranges over a range of wind forcing conditions is found to occur for $k_n u_*^2/g \approx 1\text{--}2 \times 10^{-3}$, where k_n is the wavenumber at the upper limit of the equilibrium range, u_* the friction velocity, and g the gravitational acceleration. The results are discussed in the context of Phillips' model of the equilibrium range of wind-generated gravity waves.

1. Introduction

Over the last several decades, there has been growing recognition from both oceanographic and atmospheric sciences communities that surface waves play a crucial role in the processes by which the ocean and atmosphere interact.

Until recently, most of the observational literature on surface waves was driven by studies based on time series of wave measurements at a point (or at a relatively slowly moving mooring) combined with directional information from the dynamics of the moving (pitch–roll) buoy or measurement platform. The directional and frequency response of these systems is limited and not capable of the resolution required to fully test modern theories of directional surface wave spectra. Additionally, Doppler shift

induced by longer dominant waves can distort the high-frequency portion of wave frequency spectra (Kitaigorodskii et al. 1975; Banner 1990).

It is only in the last two decades that observations of bimodal directional spectra at wavenumbers and frequencies higher than the spectral peak have been available to test numerical predictions (Banner and Young 1994; Dysthe et al. 2003; Romero and Melville 2010b; Romero et al. 2012). However, these observations are typically limited to wavenumbers and frequencies that are just a few multiples of the peak values (Hwang et al. 2000a,b; Romero and Melville 2010a), most recently up to 25 times the peak wavenumber (Leckler et al. 2015). Directional observations at higher wavenumbers, those approaching wavelengths at the lower end of the gravity wave range, are especially limited but are important as the spectrum transitions into the shorter wavelengths that are of direct relevance for many aspects of air–sea interaction and the interpretation of many remote sensing techniques. Recent improvements in image processing techniques have led

 Denotes content that is immediately available upon publication as open access.

Corresponding author: Luc Lenain, llenain@ucsd.edu

to significant progress in our ability to better understand the spatiotemporal properties of short gravity waves through stereo imagery (Leckler et al. 2015; Yurovskaya et al. 2013) or polarimetric techniques (Zappa et al. 2008), but these studies are generally limited to wavelengths shorter than a few meters because of the small field of view generally considered. Also they are potentially affected by wave reflections from the platform or ship from which the measurements are collected.

Here, we focus on directional wavenumber measurements of the surface wave field extending from kilometer down to submeter scales using airborne topographic lidar. In recent years, the development of scanning lidars along with high-precision GPS and inertial motion units (IMU) has permitted airborne measurements of the sea surface elevation with swath widths of order 100 to 1000 m under the aircraft track (Hwang et al. 2000a; Romero and Melville 2010a; Reineman et al. 2009; Melville et al. 2016), significantly improving our understanding of the physical regimes occurring over a broader range of wave scales.

The omnidirectional wavenumber spectrum $\Phi(k)$, where k is the wavenumber, computed by integrating azimuthally a directional wavenumber spectrum $\phi(k, \theta)$, where θ represents the azimuthal direction, is traditionally described by a peak wavenumber, followed by a region approximately proportional to $k^{-5/2}$ or its frequency equivalent¹ ω^{-4} , where ω is the radial frequency, referred to as the equilibrium range. This region of the wave spectrum has been extensively studied, both through analytical, spatial, and temporal observations (Donelan et al. 1985; Battjes et al. 1987; Hwang et al. 2000a; Romero and Melville 2010a; Melville et al. 2016; among others) and numerical investigation (Pushkarev et al. 2003; Romero and Melville 2010b; among others) of the wave field, more specifically of wind waves. Kitaigorodskii (1983), largely based on the pioneering work of Phillips (1958) and Kitaigorodskii (1962), suggested that the spectral form of the equilibrium range of the wind-wave spectrum was the direct consequence of a Kolmogoroff-type energy cascade from low to high frequency, combined with the existence of gravitational instabilities (breaking waves). Zakharov and Filonenko (1967) found a similar spectral shape by deriving a “wave turbulence” Kolmogoroff-type solution based on resonant interactions between weakly nonlinear surface gravity waves. In 1985, Phillips proposed a model of the equilibrium range built around the assumption that the nonlinear energy flux, wind forcing, and energy dissipation from breaking waves are in balance, proportional,

and of similar magnitude (Phillips 1985). His model also predicts a $k^{-5/2}$ spectral shape for the equilibrium range. It should also be noted that empirical parameterizations of this spectral region are also available (Toba 1973; Resio et al. 2004).

Beyond the equilibrium range, spatial and temporal observations of wind waves as well as numerical studies show a power-law transition from a $k^{-5/2}$ to a k^{-3} slope (Forristall 1981; Banner 1990; Romero and Melville 2010a,b; Romero et al. 2012), corresponding to another regime, the saturation range. Here, the primary balance is between the wind input and the dissipation from breaking waves. Observational evidence of the transition between the equilibrium and saturation ranges is very limited, as a broadband wavenumber spectrum is needed to fully resolve both regimes.

In the present study, we investigate the properties of directional wavenumber spectra of surface gravity waves, including the transition from equilibrium to saturation ranges, collected in November 2013 off the coast of California from an airborne scanning lidar installed on a research aircraft. The experiment, instrumentation, environmental conditions, and processing techniques are presented in section 2. Section 3 describes the directional properties of the wave field, including bimodality, the transition from the equilibrium to the saturation ranges, and provides some insight on the contribution of the equilibrium range to the mean square slope $\langle s^2 \rangle$ in the context of the seminal work of Cox and Munk (1954). Results are summarized in section 4.

2. Experiment

Data were collected during the Southern California 2013 (SoCal2013) experiment, an Office of Naval Research (ONR)-funded project specifically designed to collect spatiotemporal, phased-resolved measurements of wind and waves over a broad range of environmental conditions. The experiment was located between San Clemente and San Nicholas Islands (33°13.202'N, 118°58.767'W) where Research Platform (R/P) *Floating Instrument Platform (FLIP)* was moored from 7 to 22 November 2013. R/P *FLIP* was instrumented with a suite of sensors described below to characterize the atmospheric, surface, and subsurface conditions at the experiment site. A total of seven research flights are considered in the analysis, corresponding to 19.2 h on station.

a. Sea surface topography

Spatiotemporal measurements of the sea surface topography and surface kinematics were collected from a Partenavia P68 aircraft instrumented with the modular

¹ Based on the deep-water dispersion relationship.

aerial sensing system (MASS), an instrument package developed at Scripps Institution of Oceanography (SIO; Melville et al. 2016).

At the heart of the system, and of specific interest for this study, a Q680i waveform scanning lidar (Riegl, Austria) is used to make spatiotemporal measurements of the sea surface. The sensor has a maximum pulse repetition rate of 400 kHz, a maximum $\pm 30^\circ$ cross-heading raster scan rate of 200 Hz, and has been used at altitudes up to 1500 m with good returns for surface wave measurements. The theoretical swath width over water is typically proportional to the altitude of the aircraft,² and its effective width is also dependent on the wind speed and sea state. More details are available in Melville et al. (2016) and Reineman et al. (2009), the latter presenting detailed performance analysis from an earlier version of the MASS.

The MASS is also equipped with a 14-bit, 640 pixel \times 512 pixel quantum well infrared photodetector (QWIP) FLIR SC6000 infrared camera operating up to a 126-Hz frame rate in the 8.0–9.2- μm band to measure the ocean surface temperature field including modulations and gradients due to fronts, surface signatures of Langmuir circulation, and wave breaking (Sutherland and Melville 2013). A hyperspectral camera (SPECIM AisaEagle, Finland) operating in the 400–990-nm range (visible to near IR) and a JaiPulnix (San Jose, California) AB-800CL (3296 pixel \times 2472 pixel) color (24 bit) video camera that operates at a frame rate up to 17 Hz are used to provide visible imagery of the kinematics of whitecaps (Melville and Matusov 2002; Kleiss and Melville 2010, 2011; Sutherland and Melville 2013).

All data collected are carefully georeferenced from the aircraft to an earth coordinate frame using a Novatel SPAN-LN200: a very accurate GPS–IMU system combining GPS technology with an IMU using fiber-optic gyros and solid-state accelerometers to provide position and attitude data at up to 200 Hz. After differential GPS processing, using Waypoint Inertial Explorer software (Novatel Inc.), the stated accuracy for the instrument position is 0.01 m horizontal and 0.015 m (vertical), with attitude accuracies of 0.005°, 0.005°, and 0.008° for roll, pitch, and heading, respectively. A calibration–validation flight is conducted prior to and after each campaign to minimize boresight errors due to the misalignment between the GPS–IMU system and the lidar (Melville et al. 2016). Once calibrated, we typically find absolute vertical errors for the topographic product of 2 to 4 cm (per ping), estimated at 2.3 cm in the present

study from the calibration flight conducted prior to and after the experiment.

b. Environmental conditions

A suite of atmospheric sensors was installed on R/P *FLIP*'s port boom to characterize the marine atmospheric boundary layer variables used in the analysis. Wind speed and direction were measured using an array of five sonic anemometers (four CSAT3 and one Gill R3-50) mounted on a vertical telescopic mast that was deployed from the end of the port boom of *FLIP*, ranging from approximately 15 down to 2.65 m above mean sea level (MSL). The altitude above mean sea level varied during the course of the experiment, depending on environmental conditions (Grare et al. 2016), but were typically in the range of 2.6 to 4 m MSL for the lowest sensor, the Gill R3–50. The friction velocity in the air u_* is given by

$$u_* = (\overline{u'w'^2} + \overline{v'w'^2})^{1/4}, \quad (1)$$

where the covariances $\overline{u'w'}$ and $\overline{v'w'}$ are computed over 30-min records from the average cospectra for (u', w') and (v', w') . The horizontal alongwind and vertical velocities are (u, v) and w , respectively. Here, the primes indicate turbulent quantities (taken as deviations from the mean).

The Gill sonic anemometer was preferred over the Campbell model to compute the friction velocity, following the recommendations of Grare et al. (2016), who demonstrated the better performances of this unit in varying wind directions. Nevertheless, we found that during the research flights, all five sensors show consistent atmospheric friction velocity values, within 5%–10%, implying that the measurements were collected in a constant stress layer. The wind speed at 10-m height U_{10} was interpolated between the data collected at the closest measurement heights, approximately 8.5 and 14.5 m MSL, assuming a constant flux layer with a logarithmic wind profile.

Figure 1a shows the time series of wind speed U_{10} in meters per second and corresponding wind direction for the duration of the R/P *FLIP* deployment. Figure 1d shows the friction velocity u_* also in meters per second for the same period of time. Note the gray areas corresponding to the times when the aircraft was collecting data in close proximity (i.e., <10 km) to R/P *FLIP*. The wind speed, particularly variable over the duration of the experiment, ranged from approximately 1–2 to up to 11 m s^{-1} . In addition, an array of five nadir-looking laser wave gauges (MDL ILM500), located on the three booms of *FLIP*, was used to sample the directional frequency spectrum of the sea

²The swath width is close to the aircraft altitude.

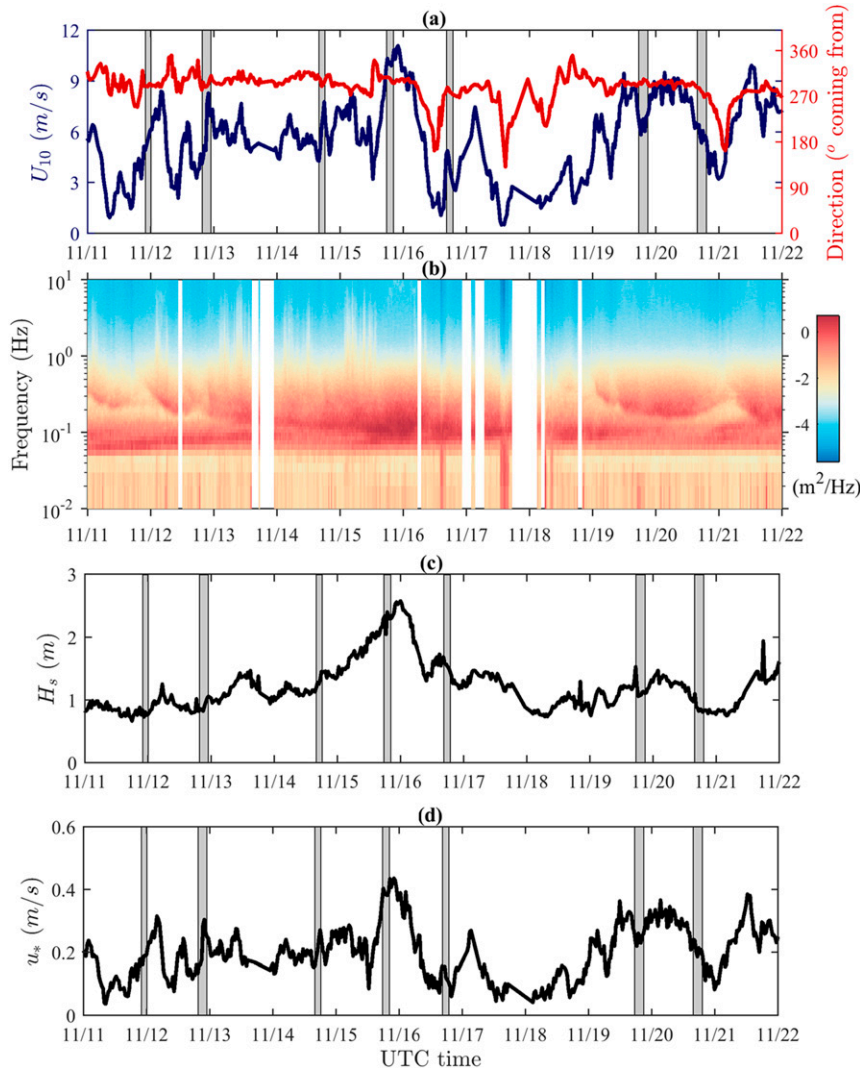


FIG. 1. Environmental conditions collected from R/P *FLIP* during the SoCal2013 experiment: (a) U_{10} (blue) and wind direction (red), (b) spectrogram of the surface displacement, (c) significant wave height H_s , and (d) atmospheric friction velocity u_* . All data points are 30-min averages. The thick gray vertical lines represent the periods of time when the aircraft was on station.

surface elevation. All wave time series were corrected for *FLIP*'s motion using a state of the art GPS-IMU: a Novatel SPAN-CPT mounted on the port boom. Figure 1b shows the spectrogram of the sea surface displacement computed for one of the wave gauges installed on the port boom. A series of short local wind events can be clearly seen, with peak energy slowly moving toward the lower frequency as the waves grow. The significant wave height H_s is shown in Fig. 1c, ranging from 0.8 to up to 2.5 m on 16 November 2013. The amplitude of the swell component in the spectra was found to be typically 1 to 2 orders of magnitude lower than the wind component. In the few cases considered in the analysis where the spectral amplitude

of the swell component was larger than that of the wind, the swell and wind seas were approximately aligned.

c. Spectral analysis

Surface elevation data collected from the MASS lidar were carefully georeferenced from aircraft to an Earth coordinate 3D point cloud. The 10-km-long swaths of data centered on R/P *FLIP* were gridded and interpolated on a regular grid, with the horizontal spatial resolution a function of the flight altitude: $dx = dy = 0.1$ m for aircraft altitude lower than 200 m MSL (typical swath width 50–150 m) and $dx = dy = 1$ m for higher altitude (typical swath width of 200–800 m). The data

collected at the edge of the swath were discarded due to high dropout rates (<10%–15% returns). Two-dimensional fast Fourier transforms were computed over 5-km segments with 50% overlap. All segments were first detrended, tapered with a two-dimensional Hanning window, and padded with zeros (25%). To correct for the Doppler shift induced by the relative motion between the phase speed of the wave and the aircraft velocity, each spectrum was corrected iteratively following the method developed by Walsh et al. (1985). The change in wavenumber component in the along-track direction is taken as

$$\delta k_x = \frac{\omega}{v_a}, \quad (2)$$

where $\omega(k)$ (rad s^{-1}) is the radial wave frequency, computed from a deep-water dispersion relationship, and v_a (m s^{-1}) is the aircraft velocity in the along-track direction.

d. Wind-wave modeling

Identifying the upper-wavenumber limit of the equilibrium range (Phillips 1985) is of obvious importance for wave modeling. Romero and Melville (2010b) and Romero et al. (2012) empirically defined this upper limit as a function of the zero-up crossing k_u of the azimuth-integrated nonlinear energy fluxes based on the requirements of Phillips' (1985) equilibrium model. In particular, Phillips' requirement that all three "source" terms be proportional excludes zero crossings if any one term is sign definite, as is dissipation. The present dataset offers a unique opportunity to test this assumption, as the measured directional wavenumber spectrum extends from the equilibrium into the saturation range. Here, the nonlinear wave–wave interaction source function S_{nl} is computed from the measured wave directional spectrum $\phi(k, \theta)$ using the so-called exact Webb–Resio–Tracy (WRT) method by Tracy and Resio (1982), based on the work by Webb (1978). We used the implementation from van Vledder (2006) used in WAVEWATCH III. Note that an αk^{-4} spectral tail (α is a constant) was added to the directional spectrum for wavenumber k larger than k_m , the wavenumber corresponding to the measured noise floor, following the methodology described in Romero et al. (2012).

3. Results

a. Bimodal structure of the directional wave spectrum

An example of a directional spectrum $\phi(k, \theta)$ from a flight conducted on 15 November 2013 is shown in Fig. 2. These data down to wavelengths of approximately 50 cm

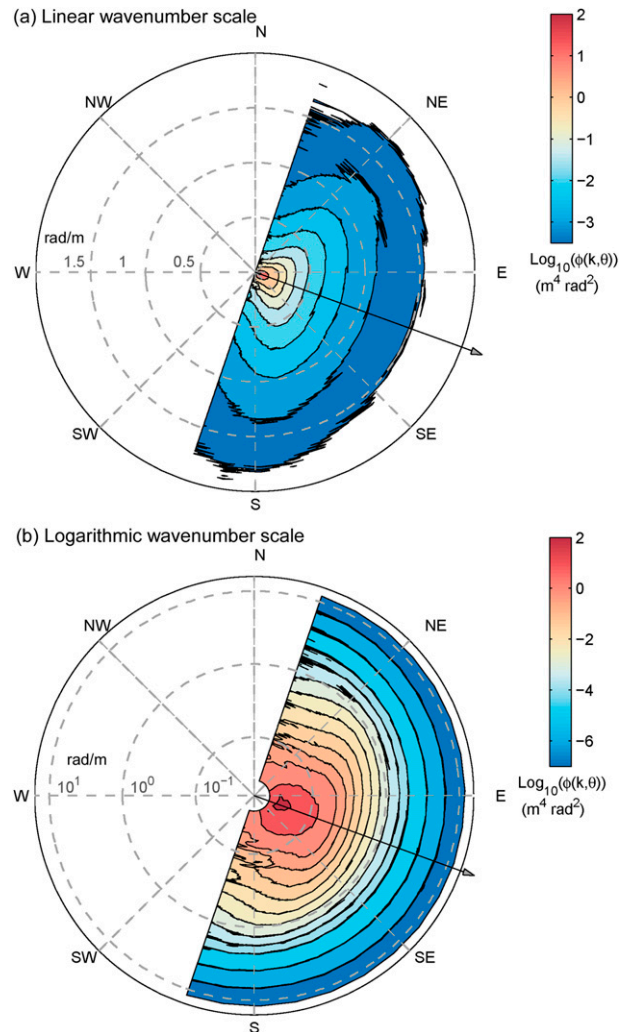


FIG. 2. Sample directional wavenumber spectrum $\phi(k, \theta)$ collected on 15 Nov 2013 during the SoCal2013 experiment (a) using a linear scale for the wavenumber k (rad m^{-1}) and (b) in log scale. Note the clear bimodal distribution, particularly evident in (a). The arrow represents the direction in which the waves at the peak wavenumber are propagating. The average wind speed U_{10} , collected on R/P FLIP, was equal to 10.2 m s^{-1} at the time of the flight. Note that for clarity, only a portion of the data, up to $1.5\text{--}2 \text{ rad m}^{-1}$, are shown in (a).

were acquired at a flight altitude of approximately 200 m. For clarity, two versions of the same directional spectrum are shown (Fig. 2a) in linear wavenumber scale, only extending to 2 rad m^{-1} to highlight the bimodal distribution and (Fig. 2b) a logarithmic wavenumber scale plot showing the full wavenumber range of the measured spectrum, extending over almost 3 decades, up to 12 rad m^{-1} . The wind speed U_{10} collected from R/P FLIP was equal to 10.2 m s^{-1} at the time of the measurements.

The bimodal distribution of the directional wave spectrum for wavenumbers larger than the spectral peak

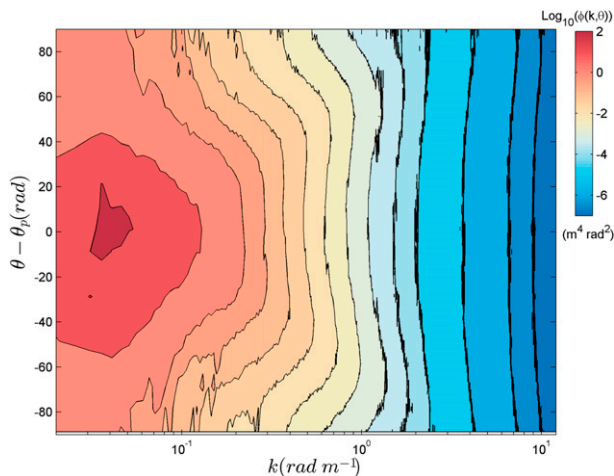


FIG. 3. The same directional wavenumber spectrum $\phi(k, \theta)$ shown in Fig. 2 collected on 15 Nov 2013 during the SoCal2013 experiment, plotted against k and relative azimuthal direction $\theta - \theta_p$. Note the clear bimodal distribution extending up to the larger values of k . An isotropic spectrum would be depicted as a vertical contour line.

has been measured in a number of past studies (Hwang et al. 2000b; Long and Resio 2007; Romero and Melville 2010a; Young 2010). Romero and Melville (2010a) found the bimodal distribution to extend out to 4–5 times the peak wavenumber k_p but were limited by the horizontal sampling resolution of the lidar they used. Similar results from a stereo imaging system installed on the Katsiveli platform (Black Sea coast of Crimea) were found recently by Leckler et al. (2015), where measurements of the bimodal distribution extended up to $k/k_p \approx 25$. In the present study, we find bimodal distributions extending up to $k/k_p \approx 100$, as shown in Fig. 3, where the directional spectrum $\phi(k, \theta)$ is plotted against normalized azimuthal direction $\theta - \theta_p$, where θ_p is the peak direction. Here, $k_p = 0.024 \text{ rad m}^{-1}$, while the bimodal peaks reach approximately $\pm 90^\circ$ at a wavenumber of approximately $3\text{--}4 \text{ rad m}^{-1}$ and remain weakly bimodal for higher wavenumbers. To our knowledge, these are the first directional wave spectrum measurements over such a broad range of scales. We define the half azimuthal separation between the two lobes as

$$\theta_{\text{lobe}}(k) = \frac{|\theta_1 - \theta_2|}{2}, \quad (3)$$

where $\theta_1(k)$ and $\theta_2(k)$ are the azimuthal angles corresponding to the two maxima of the bimodal distribution.

Figure 4 shows the azimuthal separation $\theta_{\text{lobe}}(k)$ color coded for wave age, equal to c_p/u_* , where c_p is the peak phase velocity as a function of k/k_p and the

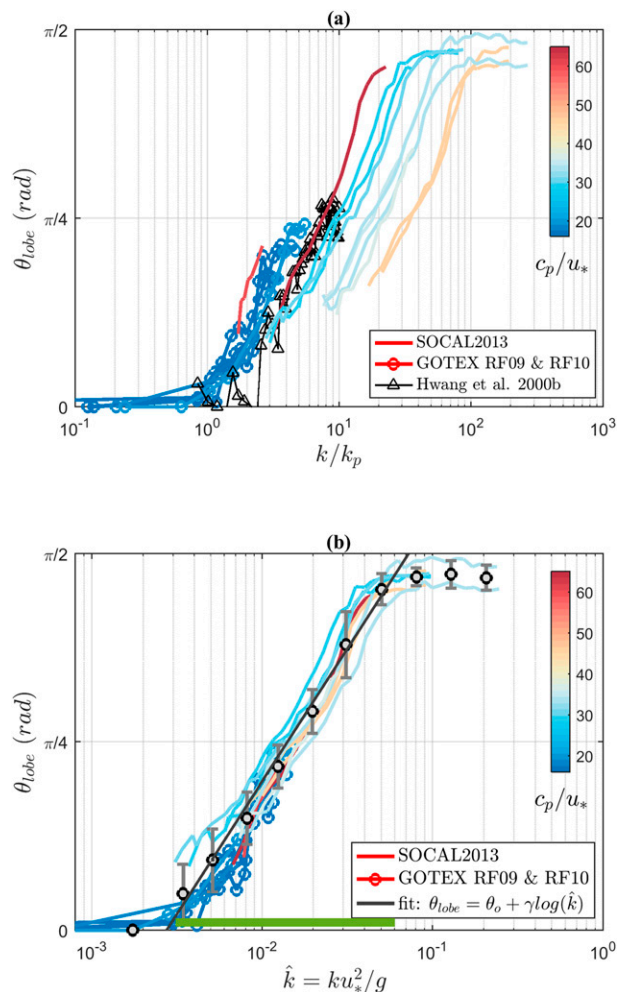


FIG. 4. Bin-averaged lobe separation θ_{lobe} plotted against (a) normalized wavenumber k/k_p and (b) nondimensional ku_*^2/g , color coded for wave age c_p/u_* for the SoCal2013 (solid line) and GOTEX (solid line with circle) experiments. RF09 and RF10 represent two of the research flights conducted during GOTEX (Romero and Melville 2010a). The black, open triangle corresponds to the measurements by Hwang et al. (2000b). An empirical fit is also shown in (b), along with bin-averaged values of the lobe separation computed over the SoCal2013 and GOTEX datasets (black circles) and corresponding error bars (one standard deviation). We find $r^2 = 0.96$ for the fit with $\theta_0 = 2.835$ and $\gamma = 0.48$. The range of validity of the fit is represented as a green horizontal bar.

nondimensional wavenumber $\hat{k} = ku_*^2/g$, following Phillips' (1985) scaling of the upper limit of the equilibrium range (top and bottom panels, respectively). Also shown are the measurements by Hwang et al. (2000b; black triangle). Data from the Gulf of Tehuantepec Experiment [GOTEX; see Romero and Melville (2010a) for details] are also plotted as solid lines with open circles.

While we find a lot of scatter in Fig. 4a, the collapse of the data in Fig. 4b is remarkable. Here, we fit the data over that range to the functional form

TABLE 1. Directional resolution for selected wavenumbers.

k (rad m ⁻¹)	0.01	0.05	0.1	0.5	1	10
$d\theta$ (rad)	6.2	1.24	0.62	0.124	0.062	0.0062

$$\theta_{\text{lobe}} = \theta_0 + \gamma \log(\hat{k}), \quad (4)$$

with $\theta_0 = 2.835$ and $\gamma = 0.48$ (coefficient of determination $R^2 = 0.96$), valid over the range $3 \times 10^{-3} < \hat{k} < 6 \times 10^{-2}$. The directional resolution of the bifurcation from a unimodal to a bimodal distribution in the neighborhood of $\hat{k} = 3 \times 10^{-3}$ and to $\theta_{\text{lobe}} = \pi/2$ in the neighborhood of $\hat{k} = 6 \times 10^{-2}$ is not sufficient to posit a functional form resolving these areas.

The lack of collapse of the azimuthal separation plotted against k/k_p is likely associated with other processes involved in the evolution of the longer wavelength portion of the spectrum (e.g., nonlinear wave–wave interactions) and measurement errors in estimating k_p .³

Also recall that the cross-track swath width is much shorter than the along-track, effectively reducing the azimuthal directional resolution $d\theta$ we can achieve for the longer waves of our spectra. Following Romero and Melville (2010a), we compute $d\theta$ as

$$d\theta = \frac{dk_2}{k}, \quad (5)$$

where dk_2 is the spectral resolution in the cross-track direction. Values of $d\theta$ for representative wavenumbers are shown in Table 1. The lack of sufficient directional resolution for the lowest wavenumbers, that is, $\hat{k} < 2\text{--}4 \times 10^{-3}$ makes the identification of a bimodal distribution for this range of wavenumbers particularly difficult.

Overall, we find that the half azimuthal separation extends well beyond what was reported in previous studies, reaching close to $\pi/2$ for the highest wavenumbers, right at the limit of what we can azimuthally resolve in the present dataset. This effectively implies that waves propagating in opposing directions can be found at scales of wavenumbers around 10–12 rad m⁻¹ or 10–11 rad s⁻¹ for linear gravity waves in the frequency domain. The existence of such wave systems has been argued to be a leading mechanism through which microseismic noise is generated (Longuet-Higgins 1950; Ardhuin et al. 2015). Space–time measurements of the evolution of the wave field are needed to explore this topic further.

The average amplitude of the lobes relative to the spectral energy in the dominant wave direction $r_{\text{lobe}}(k)$ is defined as

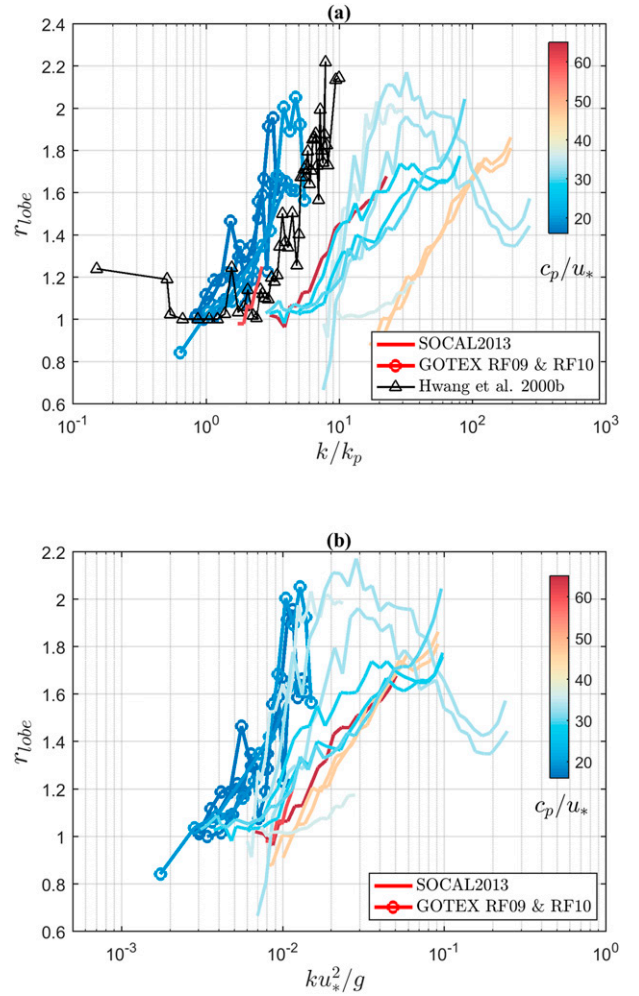


FIG. 5. Bin-averaged relative lobe amplitude r_{lobe} plotted against (a) normalized wavenumber k/k_p and (b) nondimensional ku_*^2/g , color coded for wave age c_p/u_* for the SoCal2013 (solid line) and GOTEX (solid line with circle) experiments. The black, open triangle corresponds to the measurements by Hwang et al. (2000b).

$$r_{\text{lobe}}(k) = \frac{\phi(k, \theta_1) + \phi(k, \theta_2)}{2\phi(k, 0)}. \quad (6)$$

Figure 5a shows the measured $r_{\text{lobe}}(k/k_p)$ color coded for wave age for the SoCal2013 (solid line) and GOTEX (solid line with circle) experiments. The black open triangle corresponds to the measurements by Hwang et al. (2000b). We find that r_{lobe} generally increases as a function of k/k_p , reaching $r_{\text{lobe}} \approx 2$, with a few cases showing an amplitude reduction after reaching the maxima.

Figure 5b shows $r_{\text{lobe}}(k)$ for SoCal2013 (solid line) and GOTEX (solid line with circle) experiments color coded for wave age and plotted against $\hat{k} = ku_*^2/g$. The set of curves we obtain are better collapsed than in Fig. 5a, but more work is needed to explain the remaining scatter.

³The horizontal offset is driven by k_p .

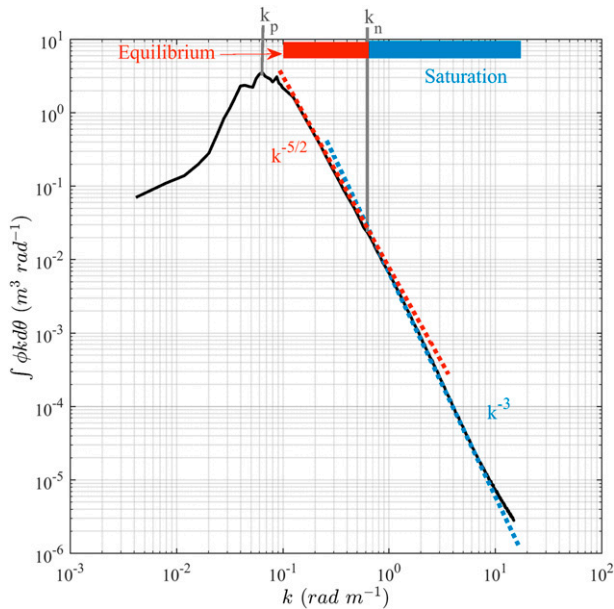


FIG. 6. Sample omnidirectional wavenumber spectrum collected on 15 Nov 2013 during the SoCal2013 experiment. Note the $-5/2$ and -3 spectral slopes and the three-decade bandwidth of the data.

b. Azimuthally integrated wave spectrum properties

Figure 6 shows the azimuthally integrated, omnidirectional spectrum computed from the directional spectrum presented in Fig. 2. The separation at wavenumber k_n of the spectral slopes into -2.5 (equilibrium) and -3 (saturation) regions is clear with $k_n = 0.6 \text{ rad m}^{-1}$ in this specific example. The first region corresponds to the equilibrium range, while the second is traditionally referred to as the saturation range (e.g., Banner et al. 1989; Banner 1990; Hwang et al. 2000a,b; Romero and Melville 2010a). Phillips (1985) proposed a model of the equilibrium range based on the assumption of balance, proportionality, and similar order of magnitude of the terms in the radiative transfer equation, namely, the wave-wave interactions, wind forcing, and wave-breaking dissipation. His model, and others, predicts a $k^{-5/2}$ slope for the equilibrium range of the omnidirectional spectrum in agreement with the present measurements.

Figure 7 shows the frequency spectrum computed from a nadir-looking lidar altimeter installed on FLIP's port boom at the same time and location the airborne lidar data shown in Fig. 6 were collected. The equilibrium and saturation ranges identified from the wavenumber spectrum are shown in red and blue, for reference, as well as the peak and transition frequencies f_p and f_n computed from k_p and k_n , assuming the deep-water dispersion relationship. While the transition is obvious in the wavenumber spectrum, the frequency

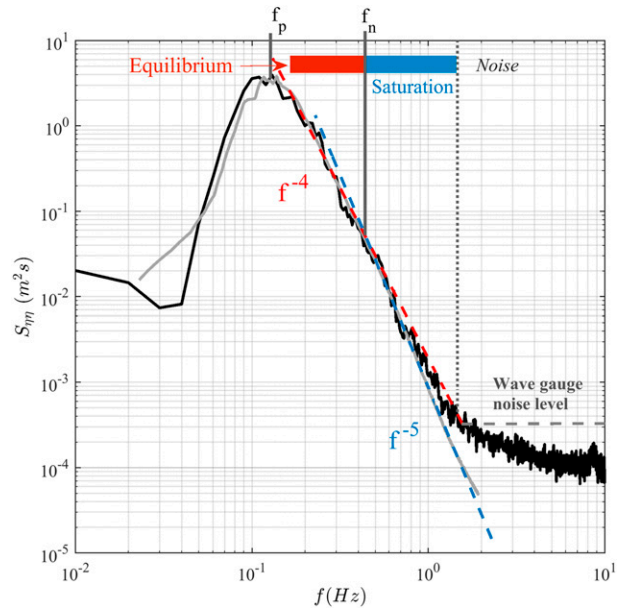


FIG. 7. Wave frequency spectrum (black) computed from a wave gauge installed on one of R/P FLIP's booms at the time when the airborne lidar data shown in Fig. 6 were collected, on 15 Nov 2015, along with the frequency spectrum (using the linear dispersion relationship) computed from the directional wavenumber spectrum (gray) used to generate Fig. 6. Also shown are the saturation and equilibrium ranges, determined from the wavenumber spectrum. While obvious in Fig. 6, and in its frequency spectrum equivalent, the transition from a f^{-4} to f^{-5} behavior is not discernable in the frequency spectrum computed from the laser wave gauge on R/P FLIP.

spectrum does not exhibit any clear change of slope between the two regimes.

Temporal point measurements are more likely to be influenced by the Doppler shift caused by the orbital motions of longer waves on the shorter waves (Kitaigorodskii et al. 1975; Banner 1990). A vertical gradient of horizontal velocity close to the surface leads to Doppler effects of varying amplitude as a function of frequency (i.e., penetration depth) and therefore has the potential to change the slope of the wave frequency spectrum. Additionally, frequency spectra measured from single-point wave gauges or buoys are generally noisier, making it harder to identify slope behavior. To illustrate this effect, we also show in Fig. 7 the frequency spectrum computed from the measured directional wavenumber spectrum (gray solid line) assuming the deep-water dispersion relationship, following Phillips (1985), where the frequency spectrum $S(\omega)$ is defined as

$$S(\omega) = 2g^{-1/2} \int_{-\pi}^{\pi} [k^{3/2} \phi(k, \theta)]_{k=\omega^2/g} d\theta. \quad (7)$$

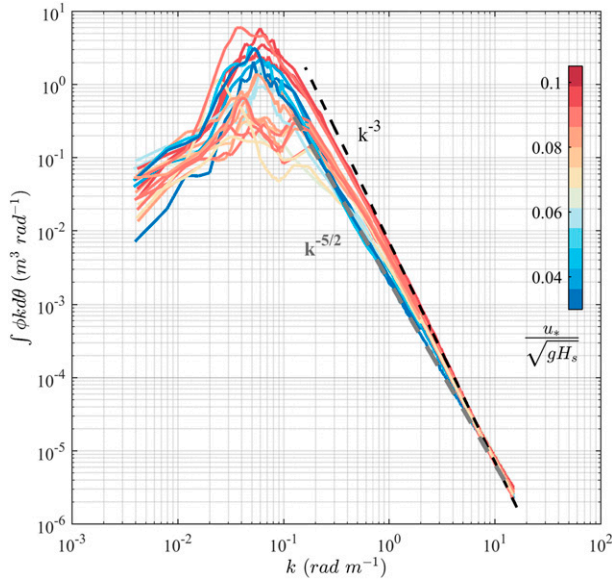


FIG. 8. Omnidirectional spectra collected during the SoCal2013 experiment, color coded for the ratio $u_*/\sqrt{gH_s}$.

This time the transition from a f^{-4} to f^{-5} power law is evident. This result reiterates the more fundamental nature of the spatial measurements of the wave field for elucidating the dynamics, as compared to the traditional parameterization of the wave field based on single-point, temporal measurements from wave gauges or buoys.

Figure 8 shows wavenumber omnidirectional spectra color coded for $u_*/\sqrt{gH_s}$ collected during the SOCAL experiment. The term $u_*/\sqrt{gH_s}$ is a nondimensional quantity corresponding to the atmospheric friction velocity scaled by the velocity $\sqrt{gH_s}$, the speed at impact of a particle following a ballistic trajectory from a height $H_s/2$. This quantity has been used to parameterize wave breaking dissipation (Drazen et al. 2008), whitecap coverage (Sutherland and Melville 2013), and more recently air entrainment by breaking waves (Deike et al. 2017). This definition was preferred to the more traditionally used wave age, equal to c_p/u_* , as c_p , the peak phase velocity, is often difficult to characterize, especially in the conditions we experienced during the experiment (a mix of swell and wind waves coming from multiple directions). Also note that in fetch-limited conditions, $c_p \propto \sqrt{gH_s}$.

We find that as $u_*/\sqrt{gH_s}$ increases, the transition between equilibrium and saturation ranges is reached at lower wavenumbers, as Phillips suggested for decreasing wave age (Phillips 1985).

c. Scaling of the saturation spectrum by the friction velocity

We introduce the azimuth-integrated saturation spectrum $B(k)$, defined as

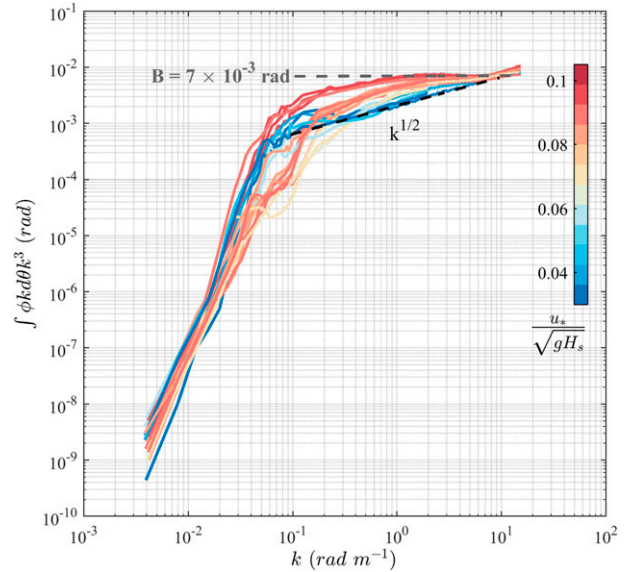


FIG. 9. Azimuth-integrated saturation spectra $B(k) = \int \phi k^4 d\theta$, collected during the SoCal2013 experiment; the curves are color coded for the ratio $u_*/\sqrt{gH_s}$.

$$B(k) = \int \phi k^4 d\theta. \tag{8}$$

The saturation spectra $B(k)$, color coded for $u_*/\sqrt{gH_s}$, computed from the directional wave spectra collected during the experiment are shown in Fig. 9. Spectral levels in the equilibrium and saturation ranges are increasing as a function of $u_*/\sqrt{gH_s}$, converging to a constant saturation level around 7 rad m^{-1} then increasing for the highest wavenumbers, up to $12\text{--}13 \text{ rad m}^{-1}$. This level increase beyond 7 rad m^{-1} could be physical, as other studies have predicted an increase of the saturation level for this range of wavenumbers. However, since it is also near the limit of the spatial resolution of the measurements, it could also be measurement noise. A subset of these saturation spectra is shown in Fig. 10, this time color coded for the wind speed U_{10} to compare the spectral saturation levels to past studies and numerical parameterization of the omnidirectional saturation spectrum. Here, we show results from stereo imagery field measurements (Banner et al. 1989; Yurovskaya et al. 2013; F. Veron 2017, personal communication), imaging slope gauge data collected in a laboratory experiment (Jähne and Riemer 1990), an empirical formulation based on field measurements from a wave gauge array (Hwang 2005), and numerical parameterization (Elfouhaily et al. 1997). While we find a lot of scatter between all these studies, the spectral levels found in the present study are generally within the range of other datasets.

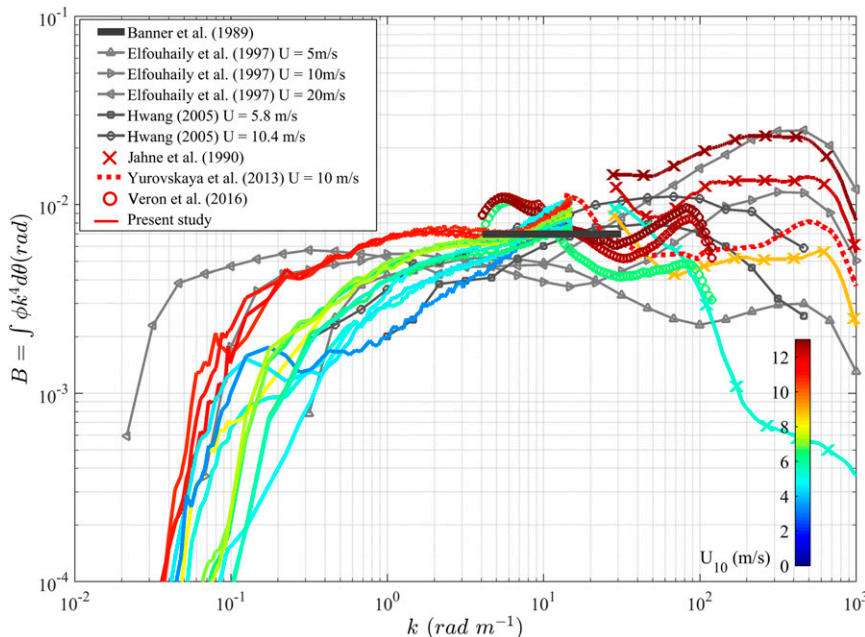


FIG. 10. Azimuth-integrated saturation spectra $B(k) = \int \phi k^4 d\theta$, collected during the SoCal2013 experiment (solid lines) and color coded for the wind speed U_{10} along with results from past observational and modeling studies.

The equilibrium range levels are consistent with the [Elfouhaily et al. \(1997\)](#) model for the larger wind speeds and [Hwang \(2005\)](#) for the intermediate wind speeds ($U_{10} = 5.8 \text{ m s}^{-1}$). The spectral levels in the saturation range are within the scatter of the other studies. Note the increase in B found for $k > 7 \text{ rad m}^{-1}$, stressing the need for field measurements of saturation spectra at higher wavenumbers.

The saturation spectra presented in [Fig. 9](#) are shown in [Fig. 11](#), also color coded for $u_* / \sqrt{gH_s}$, but this time as a function of the nondimensional wavenumber \hat{k} , following [Phillips' \(1985\)](#) scaling of the upper limit of the equilibrium range. He defines

$$k_n = rg/u_*^2, \quad (9)$$

where r is a constant.⁴ The saturation spectra collapse for nondimensional wavenumbers \hat{k} above 2×10^{-3} , both in the equilibrium ($\hat{k}^{-1/2}$, extending to $\hat{k} \approx 10^{-2}$) and saturation ranges. The transition wavenumber k_n is computed for each saturation spectrum, estimating the intersect between a $k^{-1/2}$ fit in the equilibrium range and a constant saturation value at higher wavenumbers.

⁴The term r is assumed constant for fully developed seas in [Phillips \(1985\)](#).

[Figure 12](#) shows k_n plotted against $u_* / \sqrt{gH_s}$, along with a quadratic fit of the data that gives

$$k_n = \Gamma_1 (u_* / \sqrt{gH_s})^2 - \Gamma_2 (u_* / \sqrt{gH_s}) + \Gamma_3, \quad (10)$$

where $\Gamma_1 = 1.7 \times 10^3$, $\Gamma_2 = -3.3 \times 10^2$, and $\Gamma_3 = 18$ ($R^2 = 0.94$).

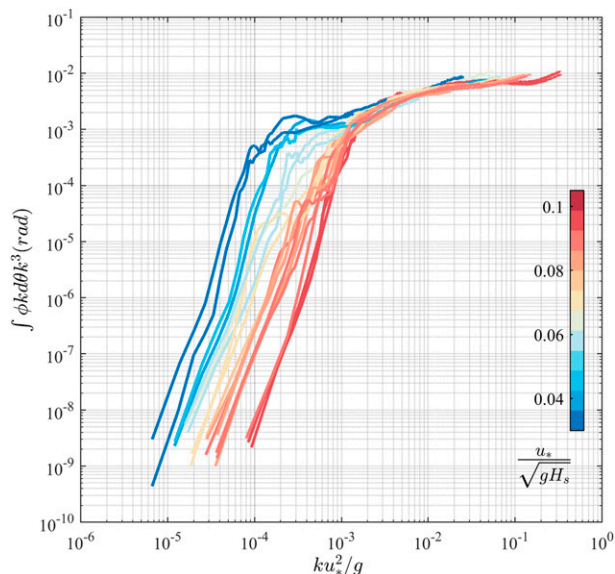


FIG. 11. Azimuth-integrated saturation spectra $B(k) = \int \phi k^4 d\theta$ plotted against $\hat{k} = ku_*^2/g$. The curves are color coded for the ratio $u_* / \sqrt{gH_s}$. Note the collapse of the spectra for the larger values of \hat{k} .

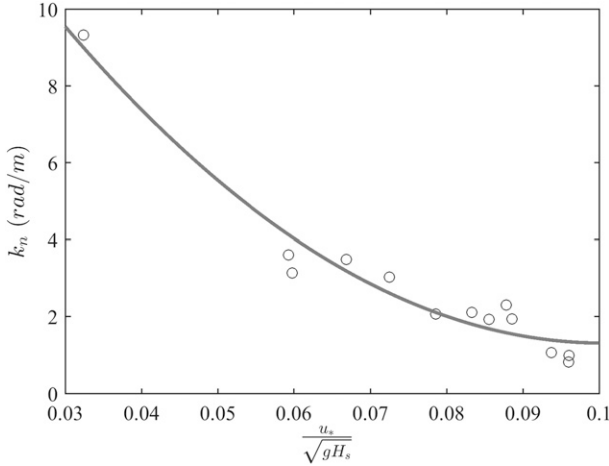


FIG. 12. The transition wavenumber k_n plotted against $u_*/\sqrt{gH_s}$.

We introduce here the nondimensional fetch χ^* , computed from the empirical formulation of Kahma and Calcoen (1992):

$$\chi^* = g\chi/u_*^2, \tag{11}$$

where χ is the fetch. Using the unstable stratification formulation based on the dimensionless peak frequency $\omega_p^* = 2\pi f_p u_*/g$,

$$\omega_p^* = 3.755(\chi^*)^{-0.287}. \tag{12}$$

Eddy flux measurements collected on R/P FLIP (L. Grare 2017, personal communications) showed the atmosphere to be unstable at the time and location where the data were collected.

We find r to vary between 0.01 and 0.025, a factor of 2.5, over the range of wave ages experienced during the field effort (Fig. 13) $30 < c_p/u_* < 120$. The value of r remains also approximately constant as a function of nondimensional fetch. Since identifying an appropriate phase speed c_p is challenging and typically requires strong assumptions, c_p is computed in two ways: from the in situ lidar measurements collected on R/P FLIP based on the wind-wave frequency spectrum peak (labeled as wind waves only) and from the peak frequency (labeled as full spectrum).

d. Nonlinear energy fluxes in equilibrium and saturation ranges

The nonlinear term S_{nl} of the radiative transport equation was computed from the measured directional wavenumber spectra assimilated into WAVEWATCH III using the implementation from van Vledder (2006). An example is shown in Fig. 14. The black arrow in the figure corresponds to the direction the waves are

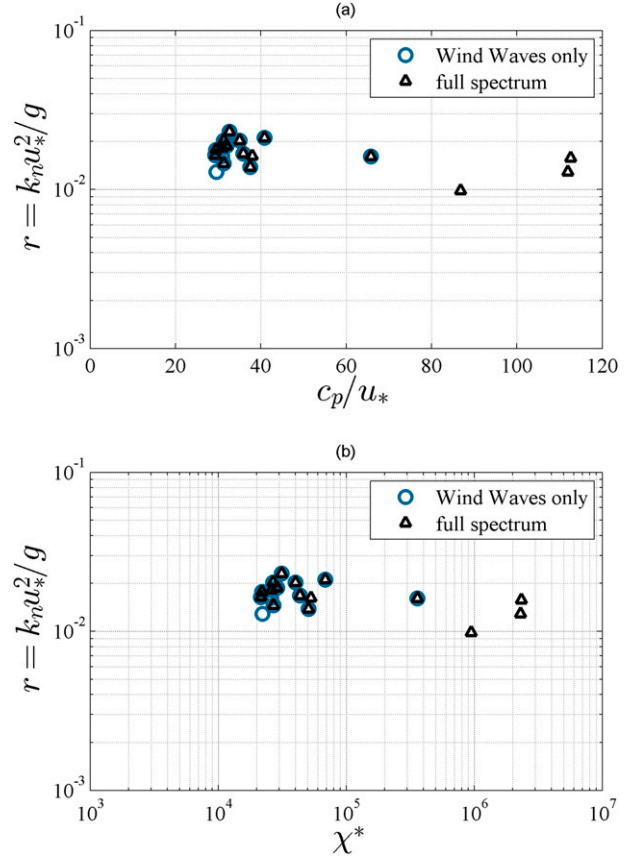


FIG. 13. The nondimensional transition wavenumber $k_n u_*^2/g$ plotted vs (a) wave age c_p/u_* and (b) the nondimensional fetch χ^* .

propagating. The value of S_{nl} is positive over the measured range of azimuth and wavenumber, but in the peak direction of wave propagation, for $k \approx 1-4 \times 10^{-1}$, S_{nl} is found to be negative. Along the same direction, for lower and higher wavenumbers, the same term is positive. The evolution of S_{nl} is consistent with the work of Romero and Melville (2010a) and Romero et al. (2012), where k_n was defined as a function of the zero-up crossing k_u of the azimuth-integrated nonlinear energy fluxes S_{nl} . This was motivated in part by Phillips' (1985) equilibrium argument, which by assuming that the three source terms were all proportional cannot include zero crossings in the nonlinear term since the wind input, under Phillips' assumptions, was positive definite.⁵ Figure 15 shows k_n plotted against its corresponding k_u , color coded for u_* . Two reference dashed lines are also shown, in blue, $k_n = 2k_u$, and in gray, $k_n = k_u$. For larger

⁵ If considering swell as well as wind waves, then the wind input term can be negative since momentum can be transferred from the waves to the wind (Hanley et al. 2010).

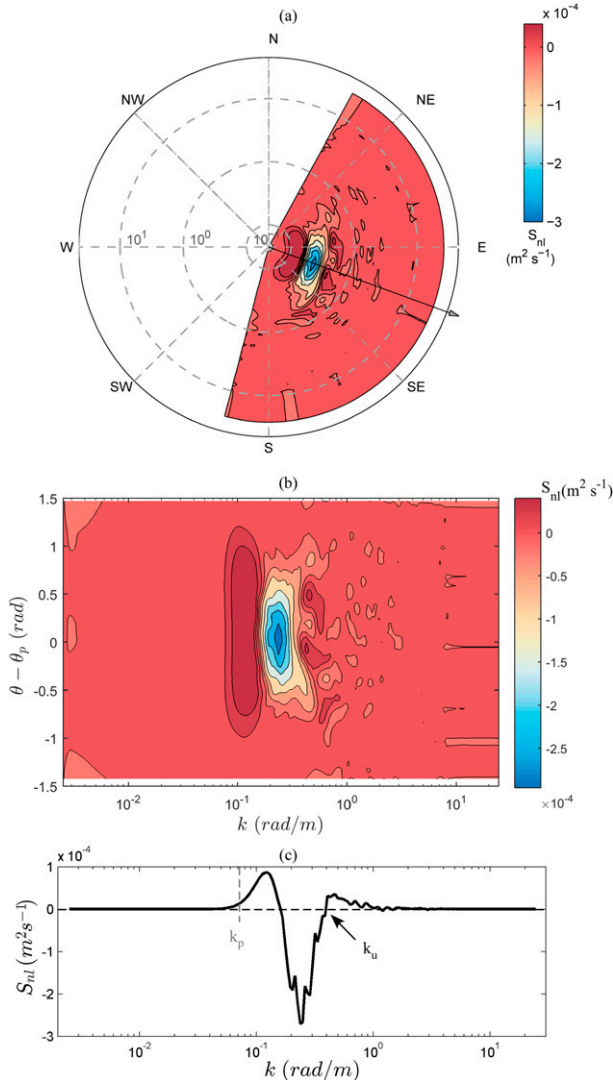


FIG. 14. Nonlinear term S_{nl} of the radiative transport equation computed from the directional wavenumber spectrum shown in Fig. 2 (a) displayed in polar coordinates and (b) plotted against k and $\theta - \theta_p$. (c) A cut through along the black arrow in (a), depicting the peak wave direction (going to). The zero-up crossing wavenumber k_u is highlighted in (c).

values of u_* , k_n is close to twice the zero-up crossing wavenumber, decreasing to a range between 1 and 2 times k_u as u_* decreases below 0.3 m s^{-1} .

The dependence of the ratio k_n/k_u over wave age is shown in Fig. 16a. Here, the wave age is computed using the peak wavenumber k_p . We find that the ratio is decreasing with wave age. A quadratic fit of the data gives

$$\frac{k_n}{k_u} = a_1 \left(\frac{c_p}{u_*} \right)^2 + a_2 \left(\frac{c_p}{u_*} \right) + a_3, \quad (13)$$

where $a_1 = 1.36 \times 10^{-4}$, $a_2 = -2.89 \times 10^{-2}$, and $a_3 = 2.43$.

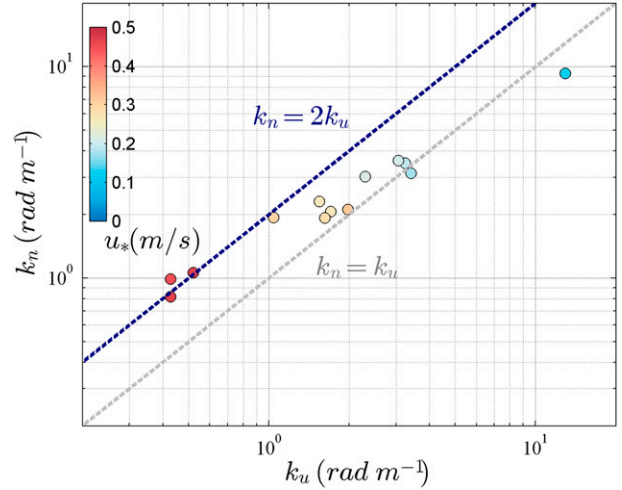


FIG. 15. Measured upper limit of the equilibrium range k_n as a function of the zero-up crossing of the nonlinear energy fluxes k_u . Each point is color coded for friction velocity u_* .

As mentioned in earlier sections, correctly identifying c_p is particularly challenging and might be misleading when the spectral peak wavenumber k_p is used. Figure 16b shows the dependence of the ratio k_n/k_u on the nondimensional quantity $u_*/\sqrt{gH_s}$. We find that the ratio is increasing with $u_*/\sqrt{gH_s}$. An exponential fit⁶ of the data gives

$$\frac{k_n}{k_u} = b_1 + b_2 e^{b_3 u_*/\sqrt{gH_s}}, \quad (14)$$

where $b_1 = 9.3 \times 10^{-1}$, $b_2 = 4.0 \times 10^{-4}$, and $b_3 = 84.4$.

e. Contribution from the equilibrium range to the total mean square slope

In deriving the total mean square slope associated with the equilibrium range, Phillips (1985) showed that r , the constant used in his study to relate k_n to u_* , is defined as

$$r = \frac{\langle s^2 \rangle}{\beta^2}, \quad (15)$$

where $\langle s^2 \rangle$ is the total mean square slope computed over the equilibrium range, from $k_o = 2.25 k_p$ to k_n , and β is Toba's constant. Here, β is computed from the equilibrium range of the omnidirectional wave spectrum, following Toba (1973), where the equilibrium range is defined as

⁶ We found a better R^2 using an exponential growth fit as opposed to a quadratic fit, 0.84 and 0.76, respectively, which motivated its use.

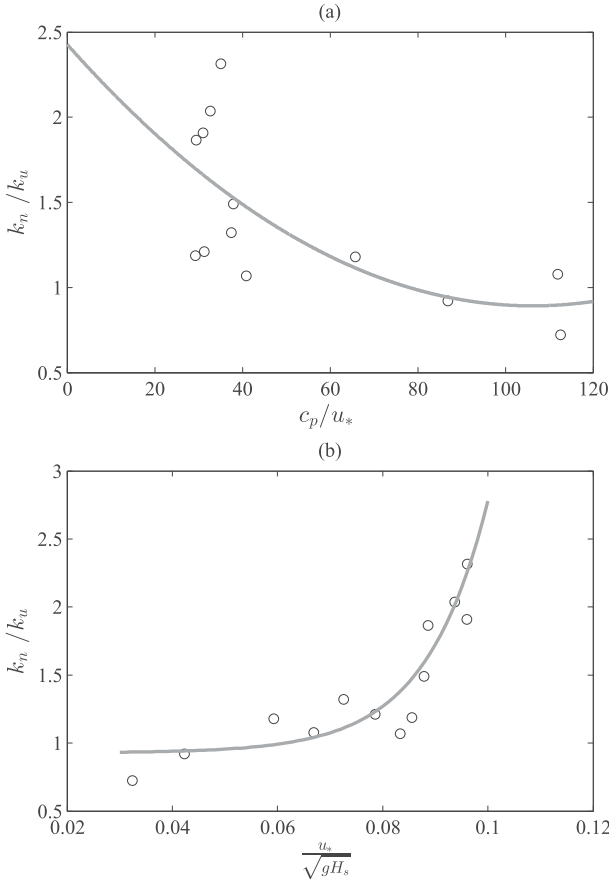


FIG. 16. Ratio k_n/k_u plotted against (a) wave age and (b) $u_*/\sqrt{gH_s}$. The gray curve shows the corresponding fits [$R^2 = 0.45$ and 0.84 for (a) and (b), respectively].

$$\Phi(k) = \frac{\beta}{2} u_* g^{-1/2} k^{-5/2}. \tag{16}$$

Toba's constant β is calculated here as

$$\beta = \frac{2g^{1/2}}{u_*} \langle \Phi(k) k^{5/2} \rangle, \tag{17}$$

where the mean compensated spectrum $\langle \Phi(k) k^{5/2} \rangle$ is computed over the equilibrium range, integrated from k_o to k_n . The low wavenumber bound was set according to Donelan et al. (1985), also used in Romero and Melville (2010a), to avoid contamination from the spectral peak.

Figure 17 shows r computed from Eqs. (9) and (15). We obtain values ranging from 0.01 to 0.025 using Eq. (9) and generally lower values using Eq. (15), ranging from 0.005 to 0.015. Using the limited observational data available at the time, Phillips concluded that $r \approx 0.3$, a value much larger than what we find in the present study. This discrepancy is not unexpected and is caused by the

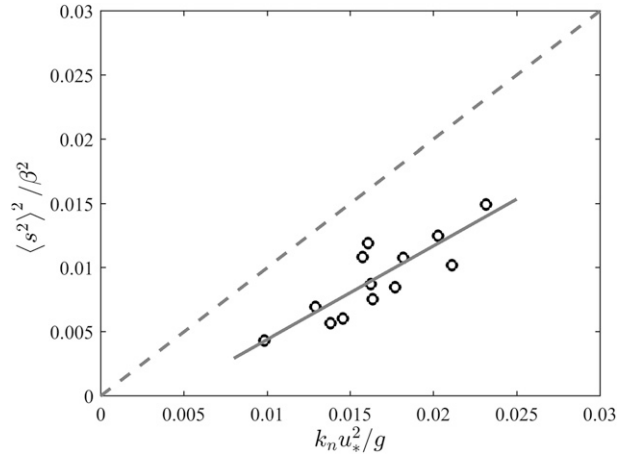


FIG. 17. Total mean squared slope squared, computed over the equilibrium range k_o to k_n , normalized by the Toba parameter (Romero and Melville 2010a) against normalized wavenumber $k_n u_*^2 / g$, following Phillips (1985). A linear fit is shown in gray, where $\langle s^2 \rangle^2 / \beta^2 = 0.73\hat{k} - 0.0029$.

fact that Phillips used Cox and Munk's (1954) classical result to compute the total mean squared slope. Their estimate, derived from airborne measurements of sun glitter, does not discriminate between equilibrium and saturation ranges. The saturation range, and beyond, in the capillary range, contributes significantly to the mean square slope, in turn leading to significant overestimation of r in Phillips' work.

In Fig. 18, we characterize the contribution of the equilibrium range to the total mean square slope. The term $\langle s^2 \rangle(k)$ is computed cumulatively based on the measured directional wave spectrum, defined as

$$\langle s^2 \rangle(k) = \int_{k_o}^k S(m) dm, \tag{18}$$

where

$$S(k) = \Phi(k) k^2. \tag{19}$$

As our reference, we use here the classical parameterization from Cox and Munk (1954), subsequently confirmed by Br on and Henriot (2006), that

$$\langle s^2 \rangle_{\text{ref}} = s_a + s_b U_{10} \pm \varepsilon, \tag{20}$$

where $s_a = 4 \times 10^{-3}$, $s_b = 5.01 \times 10^{-3}$, and $\varepsilon = 0.71 \times 10^{-3}$. Note that U_{10} was estimated from satellite scatterometry in Br on and Henriot (2006), while the wind speed in Cox and Munk (1954) was measured from an anemometer installed 12.5 m above the deck of a sailboat located at the experiment site. Each curve is color coded for friction velocity. We find that the contribution from

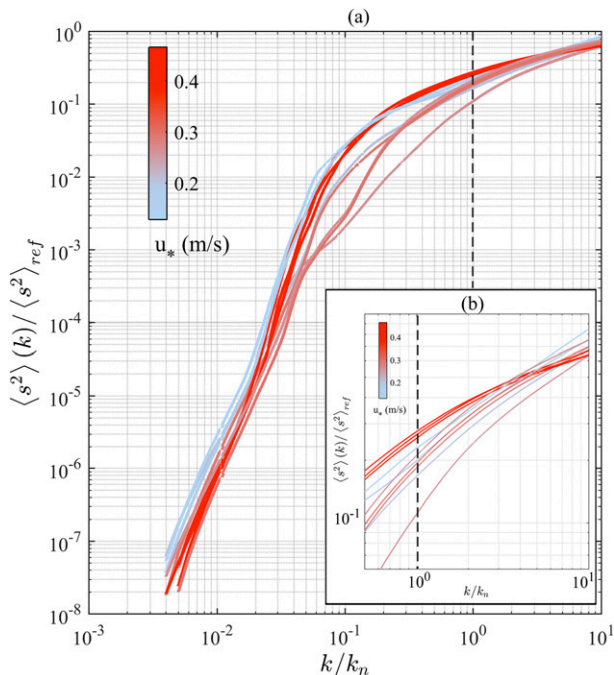


FIG. 18. (a) Total spectral mean square slope $\langle s^2 \rangle(k)$ computed from the omnidirectional wave spectrum, normalized by the total mean square slope defined by Cox and Munk (1954), $\langle s^2 \rangle_{\text{ref}}$, and plotted against the normalized wavenumber k/k_n . (b) A zoomed-in version of the same plot, focusing on the higher-wavenumber portion. The normalized wavenumber reference band $k/k_n = 1$ is shown as a black dashed line.

the equilibrium range typically corresponds to just 10%–30% of the total mean square slope.

4. Summary and discussion

Detailed topographic measurements of surface waves, ranging from kilometer to submeter scales, collected from an airborne, scanning, high-resolution waveform lidar, combined with in situ marine atmospheric boundary layer data recorded on R/P *FLIP* during the ONR SoCal2013 experiment, has provided an opportunity to characterize the directional properties of the wave field across the equilibrium saturation ranges of wind-generated surface waves and correlate them with the wind forcing. To our knowledge, this is the first study that shows directional characterization of surface waves over such a broad range of wavenumbers and environmental conditions (i.e., wind forcing).

Our measurements extend the known bimodal distribution well beyond what was reported in previous studies, with an azimuthal separation between the two lobes reaching close to π for the highest wavenumbers we could resolve, up to $k/k_p \approx 100$ –200. Though more work is needed, in particular to resolve the 180° ambiguity in the directional spectrum computed from the

lidar topographic surface wave maps, these results show that waves propagating in opposing directions can be found at wavenumbers around 10 – 12 rad m^{-1} (10 – 11 rad s^{-1} for linear gravity waves) in waves from one storm system, rather than requiring waves from opposing storms. The existence of such wave systems is believed to be a leading mechanism through which microseismic noise is generated (Longuet-Higgins 1950; Farrell and Munk 2010; Ardhuin et al. 2015).

Our measurements provide no definitive mechanism that leads to such a wide bimodal spectrum; however, there are some suggestions in the literature. From the available four-wave numerical modeling (e.g., Dysthe et al. 2003; Socquet-Juglard et al. 2005), the broadest bimodal effects have been seen out to $\pm 70^\circ$. But it is important to remember that the standard gravity wave modeling using four-wave resonance is just an asymptotic model, and for larger times and larger slopes five- and higher-wave resonances are possible. For example, in the laboratory, Su et al. (1982) and Melville (1982) showed direct evidence of the growth of crescent-shaped waves that occur at larger wave slopes and are the result of five-wave interactions leading to three-dimensional instabilities that are stronger than the two-dimensional Benjamin–Feir instabilities (McLean et al. 1981). The tails of the crescent-shaped waves propagate in almost opposing transverse directions. Wave breaking can also be a source of wave components traveling in almost transverse directions as well as upstream (Rapp and Melville 1990). In general, breaking must be considered as an omnidirectional source of high-wavenumber disturbances, but as far as we are aware there has not been any modeling of these effects. Thus, the source of the opposing transverse waves remains elusive, but the evidence presented here calls for more measurements and modeling of higher-order wave–wave interactions.

The omnidirectional wavenumber spectra show a consistent power-law behavior, proportional to $k^{-5/2}$ in the equilibrium range and k^{-3} in the saturation range. The transition between these two regimes is very well defined, and we find good agreement with the model of Phillips (1985) that predicts that the upper limit of the wavenumber in the equilibrium range is, to within a factor of 1–2, proportional to $(u_*^2/g)^{-1}$. The collapse across the equilibrium saturation ranges of the omnidirectional saturation wavenumber spectra plotted against nondimensional wavenumber \hat{k} is remarkable, as shown in Fig. 11. Note that the same scaling is also very effective in collapsing the bimodal azimuthal separation found in the directional properties of the spectra.

Direct measurements of the transition across the equilibrium and saturation regimes, over a broad range of

environmental conditions, offer an opportunity to test the empirical parameterization of k_n of Romero and Melville (2010a,b), defined as a function of the zero-up crossing wavenumber k_u of the azimuth-integrated nonlinear energy fluxes S_{nl} based on Phillips' (1985) equilibrium argument. The upper limit of the equilibrium range is indeed a function of k_u , with a clear dependence on wave age and the nondimensional atmospheric friction velocity $u_* / \sqrt{gH_s}$. This nondimensional quantity appears to be better suited in the present dataset to capture the evolution of the equilibrium saturation ranges than is the wave age.

Now able to characterize its spectral bounds, we showed that the equilibrium range of the surface wave field contributed up to 10%–30% of the total Cox and Munk (1954) mean square slope in our measurements.

Acknowledgments. The authors are grateful to Aspen Helicopter for providing flight resources, Barry Hansen for his excellent piloting during the SoCal2013 flights, and Nick Statom for collecting and processing the airborne lidar data. We are thankful to Laurent Grare for providing the atmospheric data collected from R/P FLIP and for helpful discussions. We thank Luc Deike for useful comments and suggestions on the data analysis and interpretation of the lidar data and Leonel Romero for his support with WAVEWATCH III. Fabrice Veron generously shared his data for Fig. 10. We are thankful to Luigi Cavaleri (ISMAR, Venice) and an anonymous reviewer for their suggestions, which improved the paper. This research was supported by grants to WKM from the physical oceanography programs at ONR (Grants N00014-12-1-1022 and N00014-14-1-0710) and NSF (Grants OCE-1634289 and OCE 11-55403).

REFERENCES

- Ardhuin, F., L. Gualtieri, and E. Stutzmann, 2015: How ocean waves rock the earth: Two mechanisms explain microseisms with periods 3 to 300 s. *Geophys. Res. Lett.*, **42**, 765–772, doi:10.1002/2014GL062782.
- Banner, M. L., 1990: Equilibrium spectra of wind waves. *J. Phys. Oceanogr.*, **20**, 966–984, doi:10.1175/1520-0485(1990)020<0966:ESOWW>2.0.CO;2.
- , and I. Young, 1994: Modeling spectral dissipation in the evolution of wind waves. Part I: Assessment of existing model performance. *J. Phys. Oceanogr.*, **24**, 1550–1571, doi:10.1175/1520-0485(1994)024<1550:MSDITE>2.0.CO;2.
- , I. S. Jones, and J. Trinder, 1989: Wavenumber spectra of short gravity waves. *J. Fluid Mech.*, **198**, 321–344, doi:10.1017/S0022112089000157.
- Battjes, J. A., T. J. Zitman, and L. H. Holthuisen, 1987: A reanalysis of the spectra observed in JONSWAP. *J. Phys. Oceanogr.*, **17**, 1288–1295, doi:10.1175/1520-0485(1987)017<1288:AROTSO>2.0.CO;2.
- Br on, F., and N. Henriot, 2006: Spaceborne observations of ocean glint reflectance and modeling of wave slope distributions. *J. Geophys. Res.*, **111**, C06005, doi:10.1029/2005JC003343.
- Cox, C., and W. Munk, 1954: Measurement of the roughness of the sea surface from photographs of the sun's glitter. *J. Opt. Soc. Amer.*, **44**, 838–850, doi:10.1364/JOSA.44.000838.
- Deike, L., L. Lenain, and W. K. Melville, 2017: Air entrainment by breaking waves. *Geophys. Res. Lett.*, **44**, 3779–3787, doi:10.1002/2017GL072883.
- Donelan, M. A., J. Hamilton, and W. Hui, 1985: Directional spectra of wind-generated waves. *Philos. Trans. Roy. Soc. London*, **A315**, 509–562, doi:10.1098/rsta.1985.0054.
- Drzen, D. A., W. K. Melville, and L. Lenain, 2008: Inertial scaling of dissipation in unsteady breaking waves. *J. Fluid Mech.*, **611**, 307–332, doi:10.1017/S0022112008002826.
- Dysthe, K. B., K. Trulsen, H. E. Krogstad, and H. Socquet-Juglard, 2003: Evolution of a narrow-band spectrum of random surface gravity waves. *J. Fluid Mech.*, **478**, 1–10, doi:10.1017/S0022112002002616.
- Elfouhaily, T., B. Chapron, K. Katsaros, and D. Vandemark, 1997: A unified directional spectrum for long and short wind-driven waves. *J. Geophys. Res.*, **102**, 15 781–15 796, doi:10.1029/97JC00467.
- Farrell, W. E., and W. Munk, 2010: Booms and busts in the deep. *J. Phys. Oceanogr.*, **40**, 2159–2169, doi:10.1175/2010JPO4440.1.
- Forristall, G. Z., 1981: Measurements of a saturated range in ocean wave spectra. *J. Geophys. Res.*, **86**, 8075–8084, doi:10.1029/JC086iC09p08075.
- Grare, L., L. Lenain, and W. K. Melville, 2016: The influence of wind direction on Campbell Scientific CSAT3 and Gill R3-50 sonic anemometer measurements. *J. Atmos. Oceanic Technol.*, **33**, 2477–2497, doi:10.1175/JTECH-D-16-0055.1.
- Hanley, K. E., S. E. Belcher, and P. P. Sullivan, 2010: A global climatology of wind–wave interaction. *J. Phys. Oceanogr.*, **40**, 1263–1282, doi:10.1175/2010JPO4377.1.
- Hwang, P. A., 2005: Wave number spectrum and mean square slope of intermediate-scale ocean surface waves. *J. Geophys. Res.*, **110**, C10029, doi:10.1029/2005JC003002.
- , D. W. Wang, E. J. Walsh, W. B. Krabill, and R. N. Swift, 2000a: Airborne measurements of the wavenumber spectra of ocean surface waves. Part I: Spectral slope and dimensionless spectral coefficient. *J. Phys. Oceanogr.*, **30**, 2753–2767, doi:10.1175/1520-0485(2001)031<2753:AMOTWS>2.0.CO;2.
- , —, —, —, and —, 2000b: Airborne measurements of the wavenumber spectra of ocean surface waves. Part II: Directional distribution. *J. Phys. Oceanogr.*, **30**, 2768–2787, doi:10.1175/1520-0485(2001)031<2768:AMOTWS>2.0.CO;2.
- J hne, B., and K. S. Riemer, 1990: Two-dimensional wave number spectra of small-scale water surface waves. *J. Geophys. Res.*, **95**, 11 531–11 546, doi:10.1029/JC095iC07p11531.
- Kahma, K. K., and C. J. Calkoen, 1992: Reconciling discrepancies in the observed growth of wind-generated waves. *J. Phys. Oceanogr.*, **22**, 1389–1405, doi:10.1175/1520-0485(1992)022<1389:RDITOG>2.0.CO;2.
- Kitaigorodskii, S., 1962: Applications of the theory of similarity to the analysis of wind-generated wave motion as a stochastic process. *Izv. Akad. Nauk, SSSR Ser. Geofiz.*, **1**, 105–117.
- , 1983: On the theory of the equilibrium range in the spectrum of wind-generated gravity waves. *J. Phys. Oceanogr.*, **13**, 816–827, doi:10.1175/1520-0485(1983)013<0816:OTTOTE>2.0.CO;2.
- Kitaigorodskii, S., V. Krasitskii, and M. Zaslavskii, 1975: On Phillips' theory of equilibrium range in the spectra of wind-generated gravity waves. *J. Phys. Oceanogr.*, **5**, 410–420, doi:10.1175/1520-0485(1975)005<0410:OPTOER>2.0.CO;2.

- Kleiss, J. M., and W. K. Melville, 2010: Observations of wave breaking kinematics in fetch-limited seas. *J. Phys. Oceanogr.*, **40**, 2575–2604, doi:10.1175/2010JPO4383.1.
- , and —, 2011: The analysis of sea surface imagery for whitecap kinematics. *J. Atmos. Oceanic Technol.*, **28**, 219–243, doi:10.1175/2010JTECH0744.1.
- Leckler, F., F. Ardhuin, C. Peureux, A. Benetazzo, F. Bergamasco, and V. Dulov, 2015: Analysis and interpretation of frequency–wavenumber spectra of young wind waves. *J. Phys. Oceanogr.*, **45**, 2484–2496, doi:10.1175/JPO-D-14-0237.1.
- Long, C. E., and D. T. Resio, 2007: Wind wave spectral observations in Currituck Sound, North Carolina. *J. Geophys. Res.*, **112**, C05001, doi:10.1029/2006JC003835.
- Louquet-Higgins, M. S., 1950: A theory of the origin of microseisms. *Philos. Trans. Roy. Soc. London*, **A243**, 1–35, doi:10.1098/rsta.1950.0012.
- McLean, J., Y. Ma, D. Martin, P. Saffman, and H. Yuen, 1981: Three-dimensional instability of finite-amplitude water waves. *Phys. Rev. Lett.*, **46**, 817, doi:10.1103/PhysRevLett.46.817.
- Melville, W. K., 1982: The instability and breaking of deep-water waves. *J. Fluid Mech.*, **115**, 165–185, doi:10.1017/S002212082000706.
- , and P. Matusov, 2002: Distribution of breaking waves at the ocean surface. *Nature*, **417**, 58–63, doi:10.1038/417058a.
- , L. Lenain, D. R. Cayan, M. Kahru, J. P. Kleissl, P. Linden, and N. M. Statom, 2016: The modular aerial sensing system. *J. Atmos. Oceanic Technol.*, **33**, 1169–1184, doi:10.1175/JTECH-D-15-0067.1.
- Phillips, O. M., 1958: The equilibrium range in the spectrum of wind-generated waves. *J. Fluid Mech.*, **4**, 426–434, doi:10.1017/S002212058000550.
- , 1985: Spectral and statistical properties of the equilibrium range in wind-generated gravity waves. *J. Fluid Mech.*, **156**, 505–531, doi:10.1017/S002212085002221.
- Pushkarev, A., D. Resio, and V. Zakharov, 2003: Weak turbulent approach to the wind-generated gravity sea waves. *Physica D*, **184**, 29–63, doi:10.1016/S0167-2789(03)00212-4.
- Rapp, R. J., and W. Melville, 1990: Laboratory measurements of deep-water breaking waves. *Philos. Trans. Roy. Soc. London*, **A331**, 735–800, doi:10.1098/rsta.1990.0098.
- Reineman, B. D., L. Lenain, D. Castel, and W. K. Melville, 2009: A portable airborne scanning lidar system for ocean and coastal applications. *J. Atmos. Oceanic Technol.*, **26**, 2626–2641, doi:10.1175/2009JTECH0703.1.
- Resio, D. T., C. E. Long, and C. L. Vincent, 2004: Equilibrium-range constant in wind-generated wave spectra. *J. Geophys. Res.*, **109**, C01018, doi:10.1029/2003JC001788.
- Romero, L., and W. K. Melville, 2010a: Airborne observations of fetch-limited waves in the Gulf of Tehuantepec. *J. Phys. Oceanogr.*, **40**, 441–465, doi:10.1175/2009JPO4127.1.
- , and —, 2010b: Numerical modeling of fetch-limited waves in the Gulf of Tehuantepec. *J. Phys. Oceanogr.*, **40**, 466–486, doi:10.1175/2009JPO4128.1.
- , —, and J. M. Kleiss, 2012: Spectral energy dissipation due to surface wave breaking. *J. Phys. Oceanogr.*, **42**, 1421–1444, doi:10.1175/JPO-D-11-072.1.
- Socquet-Juglard, H., K. Dysthe, K. Trulsen, H. E. Krogstad, and J. Liu, 2005: Probability distributions of surface gravity waves during spectral changes. *J. Fluid Mech.*, **542**, 195–216, doi:10.1017/S002212005006312.
- Su, M.-Y., M. Bergin, P. Marler, and R. Myrick, 1982: Experiments on nonlinear instabilities and evolution of steep gravity-wave trains. *J. Fluid Mech.*, **124**, 45–72, doi:10.1017/S002212082002407.
- Sutherland, P., and W. K. Melville, 2013: Field measurements and scaling of ocean surface wave-breaking statistics. *Geophys. Res. Lett.*, **40**, 3074–3079, doi:10.1002/grl.50584.
- Toba, Y., 1973: Local balance in the air-sea boundary processes. *J. Oceanogr. Soc. Japan*, **29**, 209–220, doi:10.1007/BF02108528.
- Tracy, B. A., and D. T. Resio, 1982: Theory and calculation of the nonlinear energy transfer between sea waves in deep water. U.S. Army Engineer Waterways Experiment Station WIS Rep. 11, 53 pp.
- van Vledder, G. Ph., 2006: The WRT method for the computation of non-linear four-wave interactions in discrete spectral wave models. *Coastal Eng.*, **53**, 223–242, doi:10.1016/j.coastaleng.2005.10.011.
- Walsh, E., D. Hancock III, D. Hines, R. Swift, and J. Scott, 1985: Directional wave spectra measured with the surface contour radar. *J. Phys. Oceanogr.*, **15**, 566–592, doi:10.1175/1520-0485(1985)015<0566:DWSMWT>2.0.CO;2.
- Webb, D., 1978: Non-linear transfers between sea waves. *Deep-Sea Res.*, **25**, 279–298, doi:10.1016/0146-6291(78)90593-3.
- Young, I., 2010: The form of the asymptotic depth-limited wind-wave spectrum: Part III—Directional spreading. *Coastal Eng.*, **57**, 30–40, doi:10.1016/j.coastaleng.2009.09.001.
- Yurovskaya, M., V. Dulov, B. Chapron, and V. Kudryavtsev, 2013: Directional short wind wave spectra derived from the sea surface photography. *J. Geophys. Res. Oceans*, **118**, 4380–4394, doi:10.1002/jgrc.20296.
- Zakharov, V., and N. Filonenko, 1967: Energy spectrum for stochastic oscillations of the surface of a liquid. *Sov. Phys. Dokl.*, **11**, 881–884.
- Zappa, C. J., M. L. Banner, H. Schultz, A. Corrada-Emmanuel, L. B. Wolff, and J. Yalcin, 2008: Retrieval of short ocean wave slope using polarimetric imaging. *Meas. Sci. Tech.*, **19**, 055503, doi:10.1088/0957-0233/19/5/055503.